A model of grain refinement and strengthening of Al alloys due to cold severe plastic deformation

Xiaoguang Qiao, N. Gao, M.J. Starink

A model of grain refinement and strengthening of Al alloys due to cold severe plastic deformation

Journal:	*Philosophical Magazine & Philosophical Magazine Letters*
Manuscript ID:	TPHM-11-Feb-0072.R2
Journal Selection:	Philosophical Magazine
Date Submitted by the Author:	19-Jul-2011
Complete List of Authors:	Qiao, Xiaoguang; University of Southampton, School of Engineering Sciences Gao, N.; Univerisity of Southampton, School of Engineering Sciences Starink, M.J.; University of Southampton; Univerisity of Southampton, School of Engineering Sciences
Keywords:	aluminium alloys, deformation, modelling, hardness, grain size
Keywords (user supplied):	Strengthening modelling, grain refinement

A model of grain refinement and strengthening of Al alloys due to cold severe plastic deformation

Xiao Guang Qiao, Nong Gao, Marco J. Starink*,
Materials Research Group, School of Engineering Sciences, University of Southampton, Southampton SO171BJ, UK

*Corresponding author. e-mail: M.J.Starink@soton.ac.uk

Abstract

This paper presents a model which quantitatively predicts grain refinement and strength/hardness of Al alloys after very high levels of cold deformation through processes including cold rolling, equal channel angular pressing (ECAP), multiple forging (MF), accumulative roll bonding (ARB) and embossing. The model deals with materials in which plastic deformation is exclusively due to dislocation movement within grains, which is in good approximation the case for many metallic alloys at low temperature, for instance aluminium alloys. In the early stages of deformation, the generated dislocations are stored in grains and contribute to overall strength. With increase in strain, excess dislocations form and/or move to new cell walls/grain boundaries and grains are refined. We examine this model using both our own data as well as the data in the literature. It is shown that grain size and strength/hardness are predicted to a good accuracy.

Key words: Al alloys, Severe plastic deformation, Grain refinement, Strengthening, modelling.

1 Introduction

Deformation to effective strains higher than about 2 is achieved in a range of processes that are either industrially relevant presently or very promising in terms of future application. Established processes include cold rolling to high strains and embossing. In addition to these, the last three decades has seen extensive research in the field of newer processes collectively named severe plastic deformation (SPD) techniques [1,2,3]. These techniques include equal channel angular pressing (ECAP), high pressure torsion (HPT) and accumulative roll bonding (ARB). One of the main advantages of these SPD techniques is that ultra high plastic deformation (with strains in the order of 10 and higher) is achieved without a substantial change in dimensions of the worked sample, thus allowing very strong grain refinement, whilst avoiding contaminations that may be introduced in other techniques [1,3].

Alloys with fine grains have many attractive properties such as good formability and superplasticity, and their strength is increased. To exploit these benefits it is crucial to understand the mechanisms of grain refinement and to have the ability to accurately predict the grain size after these high deformation processes. Ultra fine grains or even nanostructured grains (grains with size below 100 nm) can generally only be obtained if the processing temperature is limited to avoid (dynamic or static) recrystallisation. There are a number of physical models that interpret the grain refinement mechanism during SPD. Conventional dislocation theory [4,5,6,7] indicates that at the early stage of deformation a very high dislocation density is introduced, which leads to the formation of an intragranular structure consisting of cells with thick cell walls and low angles of misorientation. As the strain increases, the thickness of the cell walls decreases. These walls evolve into grain boundaries, and ultimately an array of ultra fine grains with high-angle non-equilibrium grain boundaries (GBs) [3,8] are formed. (Non-equilibrium grain boundaries may be present where there are non-geometrically necessary dislocations i.e. excess dislocations that do not contribute to the formation of misorientation at a grain boundary.) Xu et al [9] and Langdon [10] proposed a grain refinement model based on the shear band width and ECAP routes. These models describe possible mechanisms in a qualitative sense and do not predict the grain size in a quantitative way. Baik, Estrin and co-workers [11] reported a dislocation density based predictive model of the grain refinement of pure Al during ECAP. The model can accurately fit the grain size of pure Al after different passes of ECAP, but to achieve this, a range of parameters need to be fitted.

An often claimed potential advantage of SPD is that the significant grain refinement would result in significant strengthening [2,3]. However, it should also be considered that strengthening due to grain refinement is strongly material dependent: it is relatively low for Al alloys. Ashby [12], Nes and coworkers [13,14,15,16,17], Hansen and coworkers [18,19,20,21,22,23] and Estrin and co-workers [11,24] developed a number of strengthening models incorporating work hardening contributions. Ashby [12] proposed a model to predict dislocation generation due to non-shearable particles. Nes [13] studied the yield strength of conventionally deformed metallic materials during recovery through a strengthening model employing dislocation strengthening and grain boundary strengthening. Later, Nes, Marthinsen and co-workers [14,15,16,17] further expanded this model and applied it to ultra fine-grained (UFG) Al alloys processed by SPD. Hansen and co-workers [18,19,20,21,22,23] developed a strengthening model to study deformed metals, where the grain boundary strengthening follows the Hall-Petch [25,26,27] relation and dislocations are considered to store in subgrain boundaries only. Estrin and co-workers [11,24] constructed a dislocation based model in which dislocations storing in cell walls and grain interiors were considered to have the same strengthening effect. The

Estrin et al [11,24] model, in its original or slightly modified form, was extensively applied to predict strength of SPD processed alloys [28,29,30,31]. Toth et al [32] recently incorporated grain subdivision and geometrically necessary dislocations (GNDs) and further expanded this dislocation based model to predict texture, grain size, misorientation distribution and strain hardening of SPD processed alloys. These strengthening models either rely on experimental determination of several parameters (for instance, the dislocation density and the grain size in Hansen's model were obtained by EBSD measurements), or involve a number of fitted parameters (e.g. Estrin model).

The objective of the present study is to construct a model to predict the grain size and yield strength/hardness of a range of Al alloys subjected to high levels of cold plastic deformation. The model will include grain boundary strengthening, solid solution strengthening, precipitation strengthening and dislocation strengthening. Following earlier work from our group [33] we will avoid considering width of cell walls and simplify the treatment of dislocations to consider only volume average dislocation densities. The aim is to provide a transparent, computationally friendly model, with very limited number of fitted parameters as compared to the above mentioned models and verify this model by comparison to data on alloys processed by SPD and by industrially relevant cold deformation processes.

2 The model

2.1 Dislocation generations

In many metals and alloys cold plastic deformation takes place in most conditions mainly by dislocation movement. Although some deformation through twinning can occur, for example in magnesium, this only changes crystal direction to benefit the dislocation movement and does not contribute much to the overall deformation [34]. The moving dislocations may be blocked by obstacles (such as other dislocations, particles and grain boundaries), or stored in grains; and new dislocations can be generated to continue the deformation. This process was quantitatively studied by Kocks, Mecking and Estrin [35,36,37,38] through an evolution equation (the KME model):

$$\frac{d\rho_{ig}}{d\varepsilon} = (bl)^{-1} - k_2\rho_{ig} \qquad \text{Eq. 1}$$

where ρ_{ig} is the (volume averaged) dislocation density (in the grains), ε is the strain, b is the Burgers vector, l is the mean free path for dislocation movement and k_2 is a constant. The $(bl)^{-1}$ term in Eq. 1 is associated with the athermal storage of dislocations due to moving dislocations blocked by obstacles [38]. The $k_2\rho_{ig}$ term in Eq. 1 is related to the dislocation density decrease due to annihilation. We take this 'annihilation' to mean that dislocations are accumulated into grain boundaries (see Section 2.2 and [33], they are

effectively subsumed in the grain boundary). If the first term is dominant, the total dislocation density increases with strain as:

$$\rho_g = (bl)^{-1}\varepsilon \quad \text{Eq. 2}$$

We will term ρ_g the total generated dislocation density, the volume averaged dislocation density that would be obtained if no dislocations are annihilated. Eq. 2 can be alternatively obtained by the Orowan equation [39]. The volume averaged dislocation density that is stored in grains ρ_{ig} can be obtained by integrating Eq. 1:

$$\rho_{ig} = (blk_2)^{-1} - ((blk_2)^{-1} - \rho_0)e^{-k_2\varepsilon} \quad \text{Eq. 3}$$

where ρ_0 is the initial dislocation density stored in grains.
We consider the strengthening contribution of dislocations follows the classical relation [40,41,42]:

$$\Delta\tau = \alpha_1 Gb\sqrt{\rho_{ig}} \quad \text{Eq. 4}$$

$\Delta\tau$ is the shear stress increment due to dislocation density increase, α_1 is a constant, value of which is about 0.3 [41], G is the shear modulus. The relations of the shear strain and the shear stress and their equivalent counterparts of polycrystalline metals in plastic deformation are given by [43,44],

$$\frac{d\sigma}{d\tau} = \frac{d\gamma}{d\varepsilon} = M \quad \text{Eq. 5}$$

M is the Taylor factor, γ, τ are the shear strain and the shear stress and ε and σ are the equivalent strain and stress. At the early stages of deformation, dislocation generation is dominant and generated dislocations are thought to store in grains. Thus, the evolution equation of flow stress increment with equivalent strain is provided by substituting Eq. 2 in to Eq. 4:

$$\Delta\sigma = \alpha_1 MG\sqrt{\frac{b}{l}}\sqrt{\varepsilon} = K_A\sqrt{\varepsilon} \quad \text{Eq. 6}$$

Eq. 6 holds when strain is between about 0.01 to 0.05 for a range of Al alloys as well as other alloys [12]. We consider that dislocation generation during straining is continuous, and through extending application of Eq. 6 to large strain, the total volume averaged amount of dislocations generated per volume is provided by substituting Eq. 6 to Eq. 2:

$$\rho_g = \left(\frac{K_A}{\alpha_1 MGb} \right)^2 \varepsilon \qquad \text{Eq. 7}$$

K_A can be obtained experimentally through tensile test or predicted using the model described in Ref. [33]. The latter model incorporates (amongst others) Eq. 4 to Eq. 7 and also considers the contribution of the solid solute atoms to the mean free path to provide [33]:

$$K_A = C_2 GM^{3/2} b^{1/2} \left(\left[\frac{f}{2r} \right]^2 + \sum \left[B_i x_i \right]^2 \right)^{1/4} + K_A^0 \qquad \text{Eq. 8}$$

where C_2 and K_A^0 are constants, r and f are the average radius and the average volume fraction of non-shearable particles, respectively. X_i are concentrations of alloying elements i and B_i are the constants related to the relevant elements. Detailed description of the model of total generated dislocations and K_A and identification of the values of the parameters is provided in Ref. [33].

2.2 Formation of cell walls/grain boundaries

Typically, the dislocation density in grains after cold deformation at large strain (about 4 to 10) is of the order of magnitude of 10^{14} m^{-2} in Al alloys [45,46,47,48,49,50], which is two orders of magnitude lower than the generated dislocation density predicted by Eq. 7. In the KME model, the second term in the right part of Eq. 1 accounts for the difference between total generated dislocation density and dislocation density in grains. The physical essence behind this difference has been attributed to the annihilation due to recovery, but it is not clearly defined how the excess dislocations annihilate and recover [38]. We believe that annihilation of dislocations of opposite signs on the same slip plane is unlikely [33] (an exception is that it occurs when the reverse strain involved [51], but it is not the topic of the current work). Part of the dislocations generated during deformation store in grains (for instance due to being trapped by obstacles, including second phase particles and other dislocations) and the excess dislocations either form new cell walls or move to cell walls/grain boundaries. On increasing deformation, dislocations are continuously generated, and accumulate at/in the cell wall/grain boundary. During this process cell walls gradually transform into grain boundaries. Therefore, the total length of the all generated dislocations (L_g) is equal to the length of dislocations in grains (L_{ig}) plus the length of dislocations that have either formed or are accumulated in grain boundaries (L_{GB}), i.e.

$$L_g = L_{GB} + L_{ig} \qquad \text{Eq. 9}$$

The length of dislocations stored in tilt low angle grain boundaries (L_{tilt}) is related to the misorientation angle between the adjacent grains (θ) through the basic equation $\theta = b/s$ [52] in which s is the average distance between dislocations, i.e. :

$$L_{tilt} = \frac{\theta}{b} A = \frac{\theta}{b} S_v^{tilt} V \qquad \text{Eq. 10}$$

where A is boundary area, V is entire volume of the material and S_v^{tilt} is boundary area per unit volume for subgrains (cells) with tilt boundaries. Eq. 10 is valid for a tilt subgrain boundary. For a mixed tilt/twist subgrain boundary, the corresponding relation can be approximated as [18,19],

$$\rho_{cw} = \frac{L_{cw}}{V} = 1.5 \frac{\theta}{b} S_v^{cw} \qquad \text{Eq. 11}$$

where L_{cw} and ρ_{cw} are dislocation length and dislocation density stored in subgrain boundaries (cell walls), respectively. S_v^{cw} is boundary area per unit volume for subgrains (cells). The redundant dislocations in boundaries which do not contribute to the misorientation are neglected since the redundant dislocation number significantly decreases with increasing strain [18, 19]. In the present work we will consider that the latter equation also holds at least in good approximation for high angle grain boundaries (HAGBs) [33], with the dislocation density now referring to the dislocations subsumed into the grain boundary. (We will discuss this point further in Section 6.2.) Thus the density of dislocations forming/moving to cell walls/grain boundaries is taken as:

$$\frac{L_{GB}}{V} = \frac{L_g - L_{ig}}{V} = \rho_g - \rho_{ig} = \int 1.5 \frac{\theta}{b} dS_{ve} \cong 1.5 \frac{\bar{\theta}}{b} S_{ve} \qquad \text{Eq. 12}$$

where $\bar{\theta}$ is average grain boundary misorientation angle and S_{ve} is the equivalent boundary area per unit volume for refined grains formed in the deformation processing. The maximum possible value of $\bar{\theta}$ is 45° when the grains are randomly oriented [53]. The value of $\bar{\theta}$ for SPD processed Al alloys starts to approach a constant value (about 20 to 25°) after a certain strain (typically 3) [33]. Analysis of $\bar{\theta}$ data on a number of severely plastically deformed Al alloys [22,46,54,55,56,] has shown that $\bar{\theta}$ can be approximated well by [51, 57].

$$\frac{\bar{\theta}}{\bar{\theta}_m} = 1 - \left((k\varepsilon)^n / \eta + 1 \right)^{-\eta} \qquad \text{Eq. 13}$$

where n =1, and $\bar{\theta}_m$ is the maximum value that the average misorientation angle can take (45° [53]). A detailed explanation is provided in Ref [51]. Here, to simplify the equation, we take k=1 and fit the on θ for a range of alloys to obtain $\eta = 0.3$.

The boundary area per unit volume, S_v, is in practice often obtained by measuring the mean lineal intercept length, $\bar{L}$, via the fundamental relationship $S_v = 2/\bar{L}$ [58,59]. The

grain shapes are thought to resemble that following a Poisson-Voronoi tessellation [60,61,62] (see also [63,64]), and thus S_{ve} relates to the grain size as [60]:

$$S_{ve} = S_v - S_{v0} = 2.91/d_e \qquad \text{Eq. 14}$$

where S_{v0} is initial boundary area per unit volume prior to deformations, d_e is defined as the equivalent refined grain size for a material with very large starting grain size ($d_o >> d_e$). Substitution of Eq. 14 to Eq. 12 provides,

$$d_e = 4.365 \frac{\bar{\theta}}{b} \frac{V}{L_{GB}} \qquad \text{Eq. 15}$$

Thus, the equivalent refined grain size (d_e) of a material after a given strain can be calculated through substituting Eq. 3, Eq. 7, Eq. 12 and Eq. 13 to Eq. 15. (The latter equation for d_e is equivalent to the one provided in [33]. We have here derived this equation in a different way incorporating dislocation line lengths, which we believe to be clearer, and we have modified the model to incorporate dislocations in the grain.) From the above follows that the average grain size (d) after deformation is obtained through from the original grain size (d_0) and d_e as follows:

$$1/d = 1/d_0 + 1/d_e \qquad \text{Eq. 16}$$

In most cases d_0 will be substantially larger than d_e, and the size of coarse grains in the as received condition does not influence the grain size after deformation.

2.3 Hardness/yield strength of deformed Al alloys

In the present model, the yield strength of SPD processed Al alloys is taken as a superposition of grain boundary strengthening ($\Delta\sigma_{gb}$) and critical resolved shear stress (CRSS) increments caused by the intrinsic stress(τ_0), solid solute elements ($\Delta\tau_{sol}$), precipitates ($\Delta\tau_{ppt}$) and dislocations ($\Delta\tau_d$). It has been shown [54,65,66,67] that an effective way of approximating this superposition is through:

$$\sigma_y = \Delta\sigma_{gb} + M\left(\tau_0 + \Delta\tau_{sol} + \Delta\tau_{ppt} + \Delta\tau_d\right) \qquad \text{Eq. 17}$$

If no substantial ageing or precipitation occurs, $\Delta\tau_{sol}$ and $\Delta\tau_{ppt}$ are constant, and we can introduce $\sigma_0 = M(\tau_0 + \Delta\tau_{sol} + \Delta\tau_{ppt})$, which has a constant value and depends only on alloys. Eq. 17 can then be simplified to:

$$\sigma_y = \sigma_0 + \Delta\sigma_{gb} + M\Delta\tau_d \qquad \text{Eq. 18}$$

In alloys that are not precipitation hardened, σ_0 can be taken as the yield strength of the alloy in fully annealed condition. Grain boundary strengthening ($\Delta\sigma_{gb}$) may be expressed as [14,68]:

$$\Delta\sigma_{gb} = \alpha_2 Gb\left(\frac{1}{d}\right) \quad \text{Eq. 19}$$

where α_2 is a constant, d is the grain size predicted by Eq. 16. (For the present alloys both the Hall-Petch relation and the latter equation predict strengthening that is very limited as compared to other contributions [51]. This will be further discussed in Section 6.4.) The dislocation strengthening ($\Delta\tau_d$) is calculated by Eq. 4.

The Vickers hardness is expressed as [69]:

$$Hv = C\ \sigma_y \quad \text{Eq. 20}$$

where C is a constant, the value of which ranges from 3.05 to 3.28 for worked Al-1050 by conventional mechanical processing (when $Hv > 30$ HV) [54]. Here, C is taken as the average over that range, ie. C=3.16 ((For further analysis on the ratio of hardness to yield stress of metallic alloys, see [69]).

3 Materials and experimental procedure

The present study was in part carried out using data from the literature and in part on original data. The latter data was obtained from studies on Al-1050, Al-Zr and Al-Zr-Si-Fe alloys. Al-1050 is commercial purity aluminium and was supplied as an extruded rod of 9.53 mm diameter. The AlZr and AlZrSiFe alloys were supplied as plate with thickness of 12 mm and width of 60 mm, in as cast condition. The average grain sizes of these three Al alloys in as received condition is 45 µm, 690 µm and 540 µm respectively. The chemical compositions are shown in Table 1. The compositions are actual compositions obtained by chemical analysis.

The alloys were cut to rods of 65 mm in length and 9.53 mm in diameter, then processed by equal channel angular pressing (ECAP) up to 12 passes by route B_C at room temperature. The route B_C represents that the billet is rotated 90˚ in the same direction between each pass. For ECAP processing, the billet was lubricated using a suspension of MoS_2 in mineral oil, and was subsequently pressed through a die containing two channels, equal in cross-section (9.7 mm diameter), intersecting at an angle Φ=90º. The equivalent strain after one pass of ECAP is about 0.92 [70]. (Further details of the experimental set up were provided in Ref [33, 54].)

Electron backscattered diffraction (EBSD) was used to characterize the microstructure of the ECAP processed Al-1050, AlZr and AlZrSiFe alloys. Samples of 10 mm length used for EBSD analysis were machined from the centre of ECAP-processed billets. The surface of cross section was first mechanically ground up to 4000-grit SiC paper, then electropolished employing an electrolyte composed of 33 vol% nitric acid and 67 vol% methanol. The electropolishing was carried out with a DC voltage of 20-30 V for 30

seconds at -30˚C. The equipment used was a JEOL JSM6500F thermal field emission gun scanning electron microscope (FEG-SEM) equipped with an HKL EBSD detector and HKL Channel 5 software. The SEM accelerating voltage was set to 15 kV. Step size is reported with the results; in most cases it was between 0.1 and 0.5 μm. Orientation imaging microscopy (OIM) maps were obtained from the cross section perpendicular to the longitudinal direction of ECAP processed billets. The grain size was determined by an intercept method through an automated procedure. For misorientation angle distributions the lowest cut off angle was set at 2˚.

Transmission electron microscopy (TEM) was conducted on the ECAP processed AlZr alloy using a JEOL 3010 microscope operating at 300 kV. Disks of 2 mm in thickness were cut from ECAP processed billets and ground to a thickness of 0.5 mm. Subsequently, disks of 3mm in diameter were punched out, followed by twin jet polishing by an electrolyte composed of 33% nitric acid and 67% methanol at a temperature of -30˚C.

Throughout this paper we will report average grain sizes, d, as 1.455 x $\bar{L}$, where $\bar{L}$ is the average intercept length (i.e. assuming that grain shape approximates those obtained by a Poisson-Voronoi construction [60]).

Microhardness was tested using an MHT-1 model micro Vickers hardness tester. Five hardness values were measured on the cross section at the centre area of the ECAP processed billets. A force of 300g was applied and held for 15 second.

4 Experimental results

4.1 EBSD

Microstructures of the Al-1050, AlZr and AlZrSiFe alloys processed by ECAP, as characterized by EBSD, are shown in Fig.1, Fig. 2 and Fig. 3, respectively. In these figures, the grey fine lines represent grain boundaries of which the misorientation angle is between 2˚ and 15˚. Dark lines are grain boundaries with misorientation angle greater than 15˚. Misorientations less than 2˚ were ignored in order to remove the noise. The microstructure evolution of three alloys follows similar trends, i.e. after one pass of ECAP there is a strong increase in the amount of low angle grain boundaries; and with the increasing passes the fraction of high angle grain boundaries increases and the grain size decreases. The grain size of three alloys after various passes of ECAP is presented in Table 2 where grain boundaries are defined by misorientation angles greater than 2˚, and grain size was obtained by measuring the mean intercept length and converting to an average grain size.

4.2 TEM and microhardness

Fig. 4 shows TEM micrographs of the AlZr alloy after 1, 4 and 8 passes of ECAP. The shape of grains is found to develop from an elongated shape after 1 pass into an equiaxed shape, and the size of the grains decreases with increasing number of passes (i.e. with increasing accumulated plastic strain). After one single pass of ECAP, the microstructure consists of an array of band-shaped subgrains (Fig. 4 (a)). The spacing between each band is approximately 0.6μm. After 4 passes of ECAP, the band-shaped subgrains are replaced by equiaxed grains with intercept lengths of about 0.5 μm (Fig. 4 (c)) and after 8 passes of ECAP the intercept length is further refined to 0.4μm (Fig. 4 (e)). As pointed out in previous work [33], the grain size measured by TEM is slightly smaller than that measured by EBSD (see Table 2) which is due to the high resolution and omission of grain boundaries with misorientation angle smaller than 2˚ in the EBSD measurement. (For comparison with model predictions, the grain size measured by EBSD is used, as this measurement contains more grains, is statistically better defined and appears to be less susceptible to measurement errors.). Two forms of dislocation aggregates in grain boundaries were observed. One form is a parallel dislocation array (Fig. 4 (f)) and the dislocation spacing in the parallel dislocation array is very small. The other is a polygonized dislocation wall (Fig. 4 (f)), similar to those in conventionally deformed metals during recovery [71,72]. This indicates the parallel dislocation wall is the transition state between the polygonized dislocation wall and the formation of a grain boundary. In general, dislocation density is inhomogeneous.

The Vickers hardness of three alloys after different passes of ECAP is shown in Table 3. For all three alloys, the hardness increases significantly during the first pass of ECAP and increases more gradually in the subsequent passes.

5 Model predictions

5.1 Predicting the grain size and the microhardness of three alloys

The grain size of Al-1050, AlZr and AlZrSiFe after various passes of ECAP is predicted using the present model. The values of parameters used in the model are provided in Table 4. Most of the parameters (incl. α_1, α_2, b, G and M) are known at least to a good approximation and their values are taken from the literature [12,68,86,87]. The parameter determining the relation between $\overline{\theta}$ and accumulated effective strain (Eq. 13) is determined by fitting to literature data, which provides η=0.3. The value of K_A is calculated by Eq. 8. (In Ref [33] K_A predictions are verified by comparison with tensile test data.). The initial dislocation density (ρ_0), has very little influence on predictions, and is taken as 1×10^{13} m^{-2}, which is a typical value for annealed Al [73]. σ_0 is taken as the yield strength of the alloy in the annealed condition, which equals 28 MPa for Al-1050

[88], 14 MPa for AlZr and 50 MPa for ArZrSiFe. The last two values were obtained from hardness measurements, which were converted to yield strength using Eq. 20. k_2 and l are the only two parameters that are not determined from prior published data. In the present model, to determine these two parameters, we fit the model to hardness data of AlZrSiFe and calculate the root mean square error (RMSE) of the predicted hardness when tuning these two parameters. The best fitting, when RMSE reaches the minimum value, provides k_2 = 1.86 and l = 5.6 μm. k_2 is fixed throughout the present paper, i.e. it is applied to all alloys considered. The latter value of l is fixed for all commercial purity alloys with Al content higher than 99.5%.

The predicted grain sizes of the three alloys are presented in Fig. 5. The grain size here is an average value for all grains with all misorientation angles larger than 2º. (As mentioned above the grain size is defined as 1.455 times the mean intercept length, see [33]). The predicted grain size fits the measured grain size to within an average deviation of 24%. A simplified variant of this model for grain refinement (in which ρ_{ig} is neglected) has been tested against a wide range of other Al alloys, such as Al-Mg, Al-Cu, Al-7075 and Al-6082, with similar average deviations [33].

The predicted microhardness of the three alloys is shown in Fig. 6. The predicted hardness agrees very well with the experimental data.

5.2 Cold rolled Al-1200

Liu et al [22] reported data on the microstructure and the yield strength of cold rolled Al-1200 with thickness reduction from 40% to 99% (corresponding to true strains ranging from 0.5 to 5). In Fig. 7 and Fig. 8, their measured data is compared with predictions by the present model. (The experimental grain size data in Fig. 7 are measured from the TEM figures in Ref 22.) In the TEM figures [22], the grains are not equiaxed, and instead approach a rectanguloid-shape. We thus approximate their size as $d_{bw} \times d_{bw} \times \lambda_d d_{bw}$, where d_{bw} is the width of the bands, λ_d is the ratio of band length and width. Thus, Eq. 14 and Eq. 15 can be modified as:

$$S_{ve} = \sqrt[3]{\lambda_d}\,(2 + 1/\lambda_d)/d_e \qquad \text{Eq. 21}$$

$$d_e = \sqrt[3]{\lambda_d}\, d_{bw} \qquad \text{Eq. 22}$$

$$d_e = 1.5\frac{\bar{\theta}}{b}\frac{V}{L_{GB}}\sqrt[3]{\lambda_d}\left(2+\frac{1}{\lambda_d}\right) \qquad \text{Eq. 23}$$

In the model, λ_d is measured in the TEM figures [22] as 3, K_A is calculated to be 300 MPa [33], and σ_0 is taken as the yield strength in the annealed condition (19.3 MPa, see [89]). The remaining parameters are taken as the same values as Al-1050, see Table 4 for details. The l is determined as 4.5 μm by fitting. The value of l is slightly smaller than that of Al-1050 because there are more alloying elements in Al-1200 and they form more particles. The predicted grain size and yield strength fit the measured data well and the RMSE are 0.33 μm and 2.9 MPa, respectively. Fig. 8 also presents the grain boundary strengthening and the dislocation strengthening predicted by the model. Strengthening contribution of grain boundaries by Hall-Petch equation is plotted in Fig. 8 for comparison purpose. Hall-Petch constant is taken as 16 MPa $\mu m^{-1/2}$ [27].The predictions indicate dislocation strengthening is the dominant strengthening mechanism.

5.3 Al-6061 cold deformed by ECAP, multiple forging, rolling and ARB

Cherukuri et al [91] reported the microhardness of Al-6061 cold deformed by ECAP, multiple forging and ARB up to an equivalent strain of 5. This experimental data is plotted in Fig. 9, and in the same figure the hardness predicted by the present model is shown. For these predictions K_A is calculated to be 335 MPa (using the model in [33]), σ_0 is taken as is the yield strength in the annealed condition (105 MPa, see [90]). The remaining parameters are taken as the same values as Al-1050, see Table 4 for details. The only parameter that needed to be fitted is l, which is determined as 3.9 μm. The value of l is slightly smaller than that of Al-1050 and Al-1200, and this difference is thought to be caused by the fact that Al-6061 has more alloying elements. The predicted microhardness fits the measured data excellently for Al-6061 processed by ECAP and multiple forging, but the hardness of samples processed by ARB exceeds these predictions, i.e. for the same equivalent strain ARB processed Al-6061 achieves a higher hardness than Al-6061 processed by ECAP and multiple forging.

The reason for this discrepancy is thought to lie in the oxide layers and particles that are known to be introduced at the location of the bonds between the layers during ARB [90]. This will influence the hardness in two ways. Firstly, the oxide particles will cause a local increase in K_A and thus cause an enhanced grain refinement. Experimental evidence for this has been provided by Lee et al [90] who observed through TEM that the bonding area of ARB processed Al-6061 possessed a grain size that is much smaller than that away from the bonding zone. That work also confirmed the presence of a large amount of fine oxide particles observed in the bonding zone. These findings are fully consistent with our model, which indicates that the grain refinement is due to enhanced local dislocation generation around the non-shearable hard oxide particles. This grain refinement and

additional dislocation generation is one reason for the enhanced hardness. A second reason for the enhanced hardness lies in the fact that the ARB processed material effectively has become an Al6061-Al_2O_3 (laminar) metal matrix composite (see TEM figures in Ref 90) which has a higher flow strength than the Al6061 alloy. In a further paper [74] we will show that the present model can be expanded to incorporate the additional dislocation generation and grain refinement caused by the oxide particles, and that this expanded model can predict the hardness and grain size of the ARB processed alloy.

6 Discussion

The present model brings together several elements and approaches to provide a new integrated model for prediction of grain size and strength/hardness of Al alloys subjected to severe cold deformation. The approaches taken in the present model are thought to be reasonable as well as computationally efficient (and ultimately successful, see below) but it should be clearly stated that for most elements incorporated in the present integrated model alternative approaches exist. Discussing all the possible alternatives for sub-models is not realistically possible, and we will here focus on the most pertinent issues and refer to other works for further discussion and comparison.

6.1 Model accuracy and validity of model parameters

The present model accurately predicts the grain size and yield stress/hardness of a range of Al alloys after different deformation process (see Fig. 10 and Fig. 11, data of embossed Al-1050 is from Ref 75). The grain size prediction is shown to be valid for a range of alloys. The root mean square error (RMSE) for hardness prediction is 1.7 HV, and the average accuracy of grain size prediction is 25%. In the model, the mean free path, l, is the only parameter which is fitted using the experimental data. The value of l should be dependent on alloying, decreasing with increasing content of alloying/impurity elements due to increasing amount of second phase particles and precipitates in the alloys. The determined values of l for different Al alloys presented in Table 4 do indeed show this dependency, decreasing from 5.6 μm for Al-1050 (Al-0.2%Si-0.2%Fe) to 3.9 μm for Al-6061 (Al-0.9%Mg-0.7%Si-0.2%Cu-0.2Fe). A key advantage of the present model is thus that the grain size and strength of an Al alloy can be predicted after a given strain provided one single parameter, l, is obtained either experimentally, or estimated from data provided here.

The concentration of alloying elements influences model predictions in several ways. Firstly, the composition influences K_A (see Ref [33] for details), i.e. it influences rate of dislocation generation. Secondly, compositions influence strengthening contributions

though solid solution strengthening and second phase particles. In the present paper we simplified the approach by making the approximation that the size, volume fraction and distribution of the second phase particles does not change significantly during cold deformation, therefore the solid solution strengthening, precipitation strengthening and intrinsic strengthening are taken as a constant term σ_0, the value of which is assumed unchanged by deformation. This assumption is valid for alloys with a small amount of particles or particles that are already small before deformation. To improve this aspect of the model further, one would need to derive a predictive model for particle fracture and refinement during deformation.

6.2 Structure of LAGBs and HAGBs and dislocation densities

Prediction of grain size using the present model strongly relies on the relation of the average boundary area and the density of dislocations forming or joining the boundaries (see Eq. 10). Eq. 10 was originally applied to low angle tilt boundaries formed by edge dislocations and its application is here extended to high angle grain boundaries (HAGBs) (see also [33]). This approach effectively assumes that when a cell wall transforms to grain boundary, the effective total amounts of dislocations needed to obtain a certain misorientation between neighboring grains is unchanged. The misorientation angle between two adjacent grains separated by a HAGB then increases further as moving dislocations reach this HAGB and are subsumed in it. Some of the boundary structures that occur in the transition from cell walls and low angle grain boundaries (LAGBs) to HAGBs have been observed in the present TEM work (see Fig. 4 e and f). Similar TEM results of the boundary structure evolution have been reported by Chang et al [72]. Chang et al [72] observed that "on increasing strain, polygonized dislocation walls transform firstly into partially transformed boundaries, then into grain boundaries" [72], which is consistent with our model and the present EBSD results (see Fig.1, Fig. 2 and Fig. 3) which show that the fraction of LAGBs decreases with increasing strain.

Fig. 12 shows the predicted evolution of average dislocation density, ρ_{ig}, for the alloys considered in the present work, together with data on dislocation densities for selected Al alloys obtained from the literature [49,50, 76 , 77]. Fig. 12 shows that the model predictions broadly correspond with XRD determination of dislocation densities in most of the corresponding alloys. However, it is obvious that there are some deviations, and we believe that these deviations are mostly due to the following. Firstly it should be noted that XRD determinations of dislocation densities derive from measurement of microstrain from line broadening analysis [78]. These methods can not reliably analyse dislocation densities that are highly inhomogeneous. In particular, when a small volume fraction of material has a much higher dislocation density as compared to the majority of the material, then the XRD line broadening analysis will not be sensitive to the high

dislocation density areas. Secondly, TEM determinations of dislocation densities (open symbols in Fig. 12) tend to provide lower dislocation densities due to these measurements generally focusing on lower dislocation density areas, whilst also possible loss of dislocations in the sample preparation can play a role. One effect here is that in TEM sample preparation local stresses are reduced and dislocations (especially geometrically necessary dislocations) are lost. In addition, there is some uncertainty on the reliability of determination of dislocation density through EBSD. Clearly these issues related to accuracy of various dislocation density measurements need to be studied in more detail. However, when we take these points into account, Fig. 12 shows that the dislocation densities predicted by the present model are broadly in line with measured data on similar alloys, and the model broadly captures the correct trends on increasing strain.

6.3 Grain boundary misorientations

The relation between dislocation density in a cell wall or low angle grain boundary and the misorientation between the grains adopted in the present work (Eq. 10), was originally provided in the context of boundaries / cell walls with low misorientation angles [18,20]. As average misorientation angles increase to the typical values observed after SPD of about 30º we may expect that deviations will be introduced. To estimate the magnitude of possible deviations we can compare the expressions for misorientation angles for the case of dislocation that are parallel to grain boundaries. In this case the low angle approximation is [79]:

$$b/s \cong \theta \qquad \text{Eq. 24}$$

where s is the average distance between dislocations. The linear relation between θ and $1/s$ is analogous to Eq. 10. For higher angle misorientation several relations have been suggested [80,81]:

$$b/s = 2\sin(\theta/2) \qquad \text{Eq. 25}$$

or [82]

$$b/s = 2\tan(\theta/2) \qquad \text{Eq. 26}$$

or [83]

$$b/s = \tan\theta \qquad \text{Eq. 27}$$

The differences in the expressions are due primarily to different assumptions on the arrangement of dislocations in the grain boundary. A conclusive analysis as to which of these expressions (Eq. 25-Eq. 27) is more accurate is not available.

If we calculate the deviations introduced by the various approximations for a typical θ of about 30º we find deviations of 1%, -2% and 10% between Eq. 24 on the one hand and Eq. 25, Eq. 26 and Eq. 27, respectively. Thus we can expect that the adoption of the linear relation between total amount of dislocations subsumed in the grain boundary and θ, our model has an uncertainty in prediction of grain size of about 2 %, increasing to 10% if Eq. 27 would be the correct approximation. Such deviations are relatively limited (they are within the 25% accuracy in grain size predictions shown in Section 6.1) and would not significantly influence the analysis and conclusions presented here.

6.4 Grain boundary strengthening

In the present work we used the grain size strengthening equation (Eq. 19) from work by Nes and co-workers [14,68]. This approach provides a grain size strengthening that is somewhat different from the classical Hall-Petch (see e.g. [25,26,27]) approach, which is regularly invoked in a range of publications. Several possible explanations for the $d^{-1/2}$ dependency of grain size appearing in the Hall-Petch approach have been proposed (see e.g.[84,85]). To consider the possible influence of the Hall-Petch approach on model predictions we provide the following assessment.

The most complete set of data for grain size dependency of flow stress for an alloy that is similar to the alloys considered in Sections 5.1 to 5.3 is that for the Al-1050 alloy provided by Hansen [27]. Hansen's data [27] indicates a Hall-Petch constant of 25 MPa·μm$^{1/2}$ for strain ~0.2% and 7 MPa·μm$^{1/2}$ for strain 7%, with the latter strain value being a typical average strain achieved in hardness tests. Using the average on this strain range (16 MPa·μm$^{1/2}$) one would obtain an increase in yield strength of up to about 22 MPa and an increase in hardness of about 7 HV for the smallest grain sizes considered in the present work (0.5 μm). This grain size hardening is comparable to the hardening calculated using Eq. 19, thus adopting the Hall-Petch empirical equation would cause little difference. In Figs. 8 and 9 we have added the Hall-Petch type predictions, confirming differences are small.

There will be some difference due to the Hall-Petch relation containing a $d^{-1/2}$ dependency whilst Eq. 19 has a d^{-1} dependency. However, possible uncertainties introduced are thought to be limited in comparison to the overall hardening, and hence in the context of the present model and data further discussion is not fruitful. (It is also noted that for high purity Al (>99.99%) Hall-Petch constants can be 40 to 50 MPa μm$^{1/2}$

[27]. This increased Hall-Petch constant would increase the grain size strengthening effect.)

7 Conclusion

A computationally efficient model that accurately predicts the grain size and hardness of a range of Al alloys processed by cold deformation at very high strains including cold SPD is presented. Conclusions are drawn as follows:

1 The model uses very few fittable parameters, only mean free path, *l*, is fitted.
2 Parameters input in the model include the composition of an Al alloys, size of non-shearable particles and strain.
3 The model is tested using the published data of a number of Al alloys processed by ECAP, cold rolling, forging and ARB. The accuracy of the predication is good.
4 The model is applicable to the homogenous deformation of Al alloys with short and fine particles. It can be easily extended to the precipitation strengthening Al alloys with proper modifications.

Acknowledgement

This work was funded by the Engineering and Physical Sciences Research Council (EPSRC) PhD plus under Grant No. EP/P503841/1. Prof. Hans Roven (Norwegian University of Science & Technology) is gratefully acknowledged for providing selected alloys.

Table 1 Composition of the aluminium alloys used in this study

Component	Al Wt. %	Cu	Fe	Mg	Mn	Si	Ti	Zr	Zn	Other, each
Al-1050	99.65	0.01	0.18	0.01	< 0.01	0.12	0.02	-	< 0.01	< 0.01
AlZr	Bal	< 0.01	< 0.01	< 0.01	< 0.01	< 0.01	< 0.01	0.15	< 0.01	< 0.01
AlZrSiFe	Bal	< 0.01	0.19	< 0.01	< 0.01	0.17	< 0.01	0.16	0.01	< 0.01

Table 2 Average grain size, *d*, of Al-1050, AlZr and AlZrSiFe after various passes of ECAP.

Alloys	Pass number				
	1	2	4	8	12
Al-1050	2.87 μm	1.78 μm	1.47 μm	0.56 μm	0.54 μm
AlZr	3.03 μm	2.53 μm	1.89 μm	1.18 μm	
AlZrSiFe	2.87 μm	1.71 μm	1.63 μm	1.16 μm	

Table 3 Microhardness of Al-1050, AlZr and AlZrSiFe after various passes of ECAP

Alloys	Pass number					
	0	1	2	4	8	12
Al-1050	21.2 Hv	43.7 Hv	44.9 Hv	48.0 Hv	50.4 Hv	50.4 Hv
AlZr	18.7 Hv	39.2 Hv	39.9 Hv	41.3 Hv	41.1 Hv	
AlZrSiFe	29.6 Hv	50.7 Hv	53.6 Hv	57.5 Hv	61.2 Hv	

Table 4 Parameter values used in the model

Parameters	Values	Equations	Refs
α_1	0.3	Eq. 4	12
α_2	2	Eq. 19	68
b, nm	0.286	Eq. 15, Eq. 19 etc	86
C	3.16	Eq. 20	54
C_2	0.27	Eq. 8	33
G, GPa	26	Eq. 4, Eq. 19 etc	87
k	1	Eq. 13	51, 57
K_A, MPa	233 for Al-1050	Eq. 7	33
	230 for AlZr		
	238 for AlZrSiFe		
	300 for Al-1200		
	313 for Al-6061		
k_2	1.86	Eq. 1, Eq. 3	This work, by fitting to data on AlZrSiFe
l, μm	5.6 for Al-1050, AlZr and AlZrSiFe	Eq. 1, Eq. 3	This work by fitting
	4.5 for Al-1200		
	3.9 for Al-6061		
M	2.6	Eq. 17, Eq. 18	86
n	1	Eq. 13	51, 57
η	0.3	Eq. 13	51, 57
ρ_0, m^{-2}	1×10^{13}	Eq. 3	71
σ_0, MPa	28 for Al-1050	Eq. 18	88
	14 for AlZr		This work by experiment
	60 for AlZrSiFe		This work by experiment
	19.3 for Al-1200		89
	105 for Al-6061		90

Figure captions

Fig.1 Microstructure of Al-1050 from EBSD (a) in the as-received condition and processed by ECAP for (b) 1, (c) 2, (d) 4, (e) 8 and (f) 12 passes.

Fig. 2 Microstructure of AlZr alloys processed by ECAP for (a) 1, (b) 2, (c) 4 and (d) 8 passes.

Fig. 3 Microstructure of AlZrSiFe alloys processed by ECAP for (a) 1, (b) 2, (c) 4 and (d) 8 passes.

Fig. 4 TEM micrographs showing the structural evolution of AlZr alloy after (a) 1, (b) 4; (c), (d), (e) and (f) 8 passes of ECAP; (d) dark field image of a grain pointed by an arrow in (c); (e) bright field image of a grain, (f) boundary structure of the grain in (e).

Fig. 5 Measured and predicted grain sizes of Al-1050, AlZr and AlZrSiFe after different passes of ECAP at room temperature. The grain size was measured using FEG-SEM equipped with EBSD

Fig. 6 Measured and predicted microhardness of ECAP processed Al-1050, AlZr and AlZrSiFe. The error bars represent standard deviation of five measurements

Fig. 7 Prediction of grain size of cold rolled Al-1200 as a function of the rolling strain. The experimental data are from Ref 22

Fig. 8 Prediction of yield strength of Al-1200 after different strain of cold rolling. The experimental data are from Ref 22.

Fig. 9 Prediction of microhardness of Al-6061 processed by ARB, ECAP, multi-axial compression/forgings (MAC/F) and MAC/F+cold rolling. The measured Vicker's microhardness is taken from Ref 91, the arrows shown in the figure are data points of ARB. Strengthening contribution of grain boundaries by Hall-Petch equation is plotted for comparison purpose. Hall-Petch constant is taken as 16 MPa $\mu m^{-1/2}$ [27].

Fig. 10 Measured and predicted of grain size of a number of Al alloys processed by various deformation techniques. Data of Al-1050 ECAP+Embossing is from Ref 75.

Fig. 11 Measured and predicted of hardness of a number of Al alloys processed by various deformation techniques. Data of Al-1050 ECAP+Embossing is from Ref 75.

Fig. 12 Prediction of densities of dislocations generated (DG) during deformations and dislocations stored in grains (IG). Experimental data for pure Al (ECAP, XRD), Al-1050 (rolling, EBSD), Al-1100 (ARB, TEM), Al-6082 (ECAP, XRD) and Al-Mg (ECAP, XRD) are from Refs [50,76,77,49 and 50], respectively.

Reference:

[1] R.Z. Valiev, Y. Estrin, Z. Horita, T.G. Langdon, M.J. Zehetbauer and Y.T. Zhu, JOM 58 (2006) p. 33.
[2] R.Z. Valiev and T.G. Langdon, Prog Mater Sci 51 (2006) p. 881.
[3] R.Z. Valiev, R.K. Islamgaliev and I.V. Alexandrov, Prog Mater Sci 45 (2000) p. 103.
[4] R.Z. Valiev, Y.V. Ivanisenko, E.F. Rauch and Baudelet, Acta Mater 44 (1996) p. 4705.
[5] J. Gil Sevillano and E. Aernoudt, Mater Sci Eng A 86 (1987) p. 35.
[6] A.S. Argon and P. Haasen, Acta Metall Mater 41 (1993) p. 3289
[7] A.D. Rollett and U.F. Kocks, Solid State Phenomena 35–36 (1994) p. 1
[8] R.Z. Valiev, Nat Mater 3 (2004) p. 511.
[9] C. Xu, M. Furukawa, Z. Horita and T.G. Langdon, Mater Sci Eng A 398 (2005) p. 66.
[10] T.G. Langdon. Mater Sci Eng A 462 (2007) p. 3.
[11] S.C. Baik, Y. Estrin, H.S. Kim and R.J. Hellmig. Mater Sci Eng A 351 (2003) p. 86
[12] M.F. Ashby. The Deformation of Plastically Non-Homogeneous Alloys, in: Kelly A, Nicholson RB(Eds), Strengthening Methods in Crystals, Amsterdam: Elsevier; 1971.
[13] E. Nes. Acta Metal Mater 43 (1995) p. 2189.
[14] K. Marthinsen and E. Nes. Mater Sci Eng A 234–236 (1997) p. 1095.
[15] E. Nes and K. Marthinsen. Mater Sci Eng A 322 (2002) p. 176.
[16] O. Nijs, B. Holmedal, J. Friis and E. Nes. Mater Sci Eng A 483-484 (2008) p. 51.
[17] E. Nes, B. Holmedal, E. Evangelista and K. Marthinsen. Mater Sci Eng A 410-411 (2005) p. 178.
[18] N. Hansen. Scripta Mater 51 (2004) p. 801.
[19] D.A. Hughes, N. Hansen and D.J. Bammann. Scripta Mater 48 (2003) p. 147.
[20] J.R. Bowen, P.B. Prangnell, D. Juul Jensen and N. Hansen. Mater Sci Eng A 387-389 (2004) p. 235.
[21] N. Kamikawa, X. Huang, N. Tsuji and N. Hansen. Acta Mater 57 (2009) p. 4198.
[22] Q. Liu, X. Huang, D.J. Lloyd and N. Hansen. Acta Mater 50 (2002) p. 3789.
[23] X. Huang, N. Kamikawa and N. Hansen. Mater Sci Eng A 483-484 (2008) p.102.
[24] Y. Estrin, L.S. Toth, A. Molinari and Y. Brechet, Acta Mater 46 (1998) p. 5509.
[25] E.O. Hall, Proc Phys Soc Sect B 64 (1951) p. 747.
[26] N.J. Petch, J Iron Steel Inst 26 (1953) p. 601.
[27] N. Hansen. Acta Metall 25 (1977) p. 863.
[28] O. Rezvanian, M.A. Zikry. J Eng Mater Technol 131 (2009) p. 011002.
[29] V. Lemiale, Y. Estrin, H.S. Kim, R. O'Donnell. Comput Mater Sci 48 (2010) p. 24.
[30] E. Hosseini, M. Kazeminezhad. Comput Mater Sci 44 (2009) p. 962.
[31] E. Chen, L. Duchene, A.M. Habraken, B. Verlinden. Rev Adv Mater Sci 25 (2010) p. 23.
[32] L.S. Toth, Y. Estrin, R. Lapovok and C. Gu. Acta Mater 58 (2010) p.1782.
[33] M.J. Starink, X.G. Qiao, J. Zhang, N. Gao. Acta Mater 57 (2009) p.5796.
[34] J.W. Christian, S. Mahajan. Prog Mater Sci 39 (1995) p. 1.
[35] U.F. Kocks. Phil Mag 13 (1966) p. 541.
[36] H. Mecking, U.F. Kocks. Acta Metall Mater 29 (1981) p.1865.
[37] U.F. Kocks, H. Mecking. Prog Mater Sci 48 (2003) p. 171.
[38] Y. Estrin, H. Mecking. Acta Metall Mater 32 (1984) p. 57.

[39] E. Orowan, Z. Physik 89, (1934) p. 605, 614, 634.
[40] G.I. Taylor. Proc. Roy. Soc., A 145 (1934) p. 362.
[41] M.F. Ashby, Phil Mag 21 (1970) p. 399.
[42] S.C. Wang, Z. Zhu and M.J. Starink. J Microscopy 217 (2005) p. 174.
[43] J.F.W. Bishop, R. Hill. Phil Mag 42 (1951) p. 414.
[44] N. Kamp, I. Sinclair I, M.J. Starink. Metall Mater Trans A 33A (2002) p. 1125.
[45] M.A. Munoz Morris, I. Gutierrez-Urrutia and D.G. Morris, Mater Sci Eng A 493 (2008) p. 141.
[46] M. Reihanian, R. Ebrahimi, M.M. Moshksar, D. Terada, N. Tsuji. Mater Char 59 (2008) p. 1312.
[47] J. Gubicza, N.Q. Chinh, Z. Horita, T.G. Langdon. Mate Sci Eng A 387-389 (2004) p. 55.
[48] Y.H. Zhao, X.Z. Liao, Z. Jin, R.Z. Valiev, Y.T. Zhu. Acta Mater 52 (2004) p.4589.
[49] S.G. Chowdhury, A. Mondal, J. Gubicza, G. Krallics, A. Fodor. Mater Sci Eng A 490 (2008) p. 335.
[50] J. Gubicza, N.Q. Chinh, Gy. Krallics, I. Schiller and T. Ungar. Curr Appl Phys 6 (2006) p. 194.
[51] J. Zhang, M.J. Starink, N. Gao. Mater Sci Eng A 528 (2011) p. 2581.
[52] J.M. Burgers. Proc. K. Ned. Akad. Wet 42 (1939) p. 293.
[53] J.K. Mackenzie, M.J. Thomson. Biometrika 44 (1957) p. 205.
[54] X.G. Qiao, M.J. Starink, N. Gao. Mater Sci Eng A 513 (2009) p. 52.
[55] E.A. El-Danaf. Mater Sci Eng A 487 (2008) p. 89.
[56] E.A. El-Danaf, M.S. Soliman, A.A. Almajid, M.M. El-Rayes, Mater Sci Eng A 458 (2007) p. 226.
[57] M.J. Starink. Int Mater Rev 49 (2004) p. 191.
[58] J.J. Friel. Practical guide to image analysis, Materials Park OH: ASM International; 2000.
[59] E.E. Underwood. Quantitative stereology, Reading MA: Addison-Wesley; 1970.
[60] A. Thorvaldsen. Acta Mater 45 (1997) p.587.
[61] A. Thorvaldsen. Acta Mater 45 (1997) p.595.
[62] F. Yin, A. Sakurai, X. Song, Metall Mater Trans A 37 (2006) p. 3707.
[63] B. Regener, C. Krempaszky, E. Werner, M. Stockinger, Comput Mater Sci, In Press, DOI: 10.1016/j.commatsci.2011.03.035.
[64] M. Velasco, H. Van Swygenhoven, C. Brandl, Scripta Mater 65 (2011) p. 151
[65] M.J. Starink, S.C. Wang. Acta Mater 51 (2003) p.5131.
[66] M.J. Starink, A. Deschamps, S.C. Wang, Scripta Mater 58 (2008) p. 377.
[67] M.J. Starink, S.C. Wang, Acta Mater 57 (2009) p. 2376.
[68] E. Nes, T.K. Pettersen, K. Marthinsen. Scripta Mater 43 (2000) p. 55.
[69] X.G. Qiao, N. Gao, M.J. Starink. Acta Mater 58 (2010) p. 3690.
[70] Y. Iwahashi, J.T. Wang, Z. Horita, M, Nemoto, T.G. Langdon, Scripta Mater 35 (1996) p. 143.
[71] F.J. Humphreys, M. Hatherly. Recrystallization and related annealing phenomena, second ed. Oxford: Pergamon;2004.
[72] C.P. Chang, P.L. Sun, P.W. Kao. Acta Mater 48 (2000) p. 3377.
[73] T.N. Lipchin, A.P. Nishta. Met Sci Heat Treat 22 (1980) p. 601.

[74] X.G. Qiao, N. Gao. M.J. Starink. Submitted to J. Mater. Sci.
[75] X.G. Qiao, N. Gao, M.J. Starink. http://eprints.soton.ac.uk/185111/
[76] C.C. Merriman, D. P. Field, P. Trivedi. Mater Sci Eng A 494 (2008) p. 28.
[77] Y. Miyajima, M. Mitsuhara, S. Hata, H. Nakashima, N. Tsuji. Mater Sci Eng A 528 (2010) p. 776.
[78] T. Ungár, J. Gubicza, G. Ribárik, A. Borbély. J Appl Cryst 34 (2001) p. 298.
[79] A.W. Sleeswyk. Acta Metall 11 (1963) p. 1192.
[80] W.T. Read. Dislocations in Crystals, McGraw-Hill: New York; 1953.
[81] J. Friedel. Les Dislocations, Gauthier-Villars: Paris; 1956.
[82] A.H. Cottrell. Dislocations and Plastic Flow in Crystals, Clarendon: Oxford; 1953.
[83] Y. Estrin, L.S. Tóth, Y. Brechet, H.S. Kim. Mater Sci Forum 503–504 (2006) p. 675.
[84] R.W. Cahn, P. Haasen, Physical Metallurgy, second ed. Amsterdam: North-Holland; 1983.
[85] V Bata, E.V. Pereloma, Acta Mater. 52 (2004) p. 657.
[86] J.W. Hutchinson. Proc R Soc London A 319 (1970) p. 247.
[87] J.R. Kissell, R.L. Ferry. Aluminium structures: a guide to their specifications and design, second ed. New York: John Wiley&Sons;2002.
[88] ASM handbook. Vol. 2, Properties and selection: nonferrous alloys and special-purpose materials, tenth ed., ASM international. 1991.
[89] Ø. Ryen, B. Holmedal, O. Nijs, E. Nes, E. Sjölander, H.E. Ekström. Metal Mater Trans A 37A (2006) p. 1999.
[90] S.H. Lee, Y. Saito, T. Sakai, H. Utsunomiya. Mater Sci Eng A 325 (2002) p. 228.
[91] B. Cherukuri, T.S. Nedkova, R. Srinivasan. Mater Sci Eng A 410–411 (2005) p.394.

Fig 1

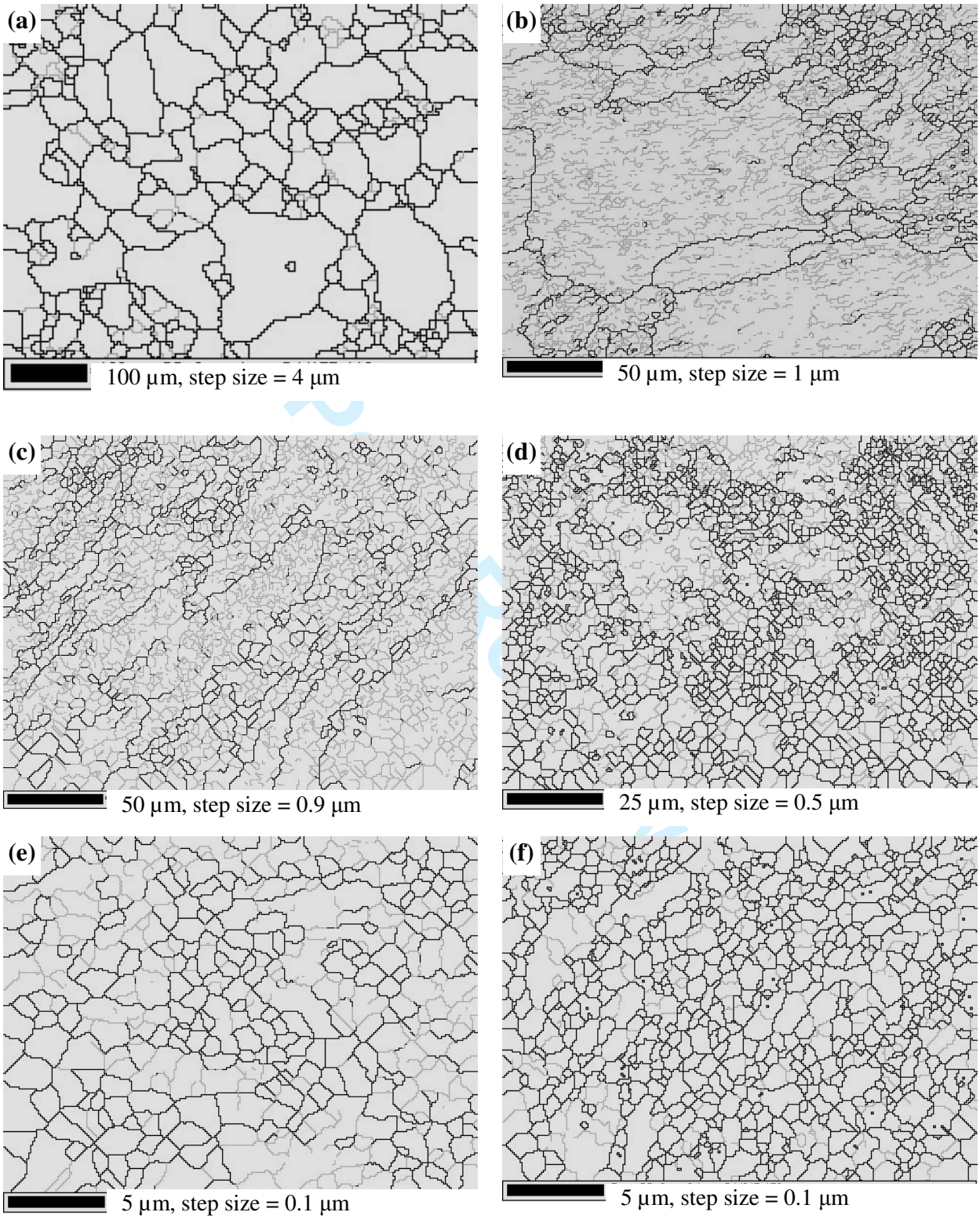
(a)
100 µm, step size = 4 µm
(b)
50 µm, step size = 1 µm
(c)
50 µm, step size = 0.9 µm
(d)
25 µm, step size = 0.5 µm
(e)
5 µm, step size = 0.1 µm
(f)
5 µm, step size = 0.1 µm

Fig 2

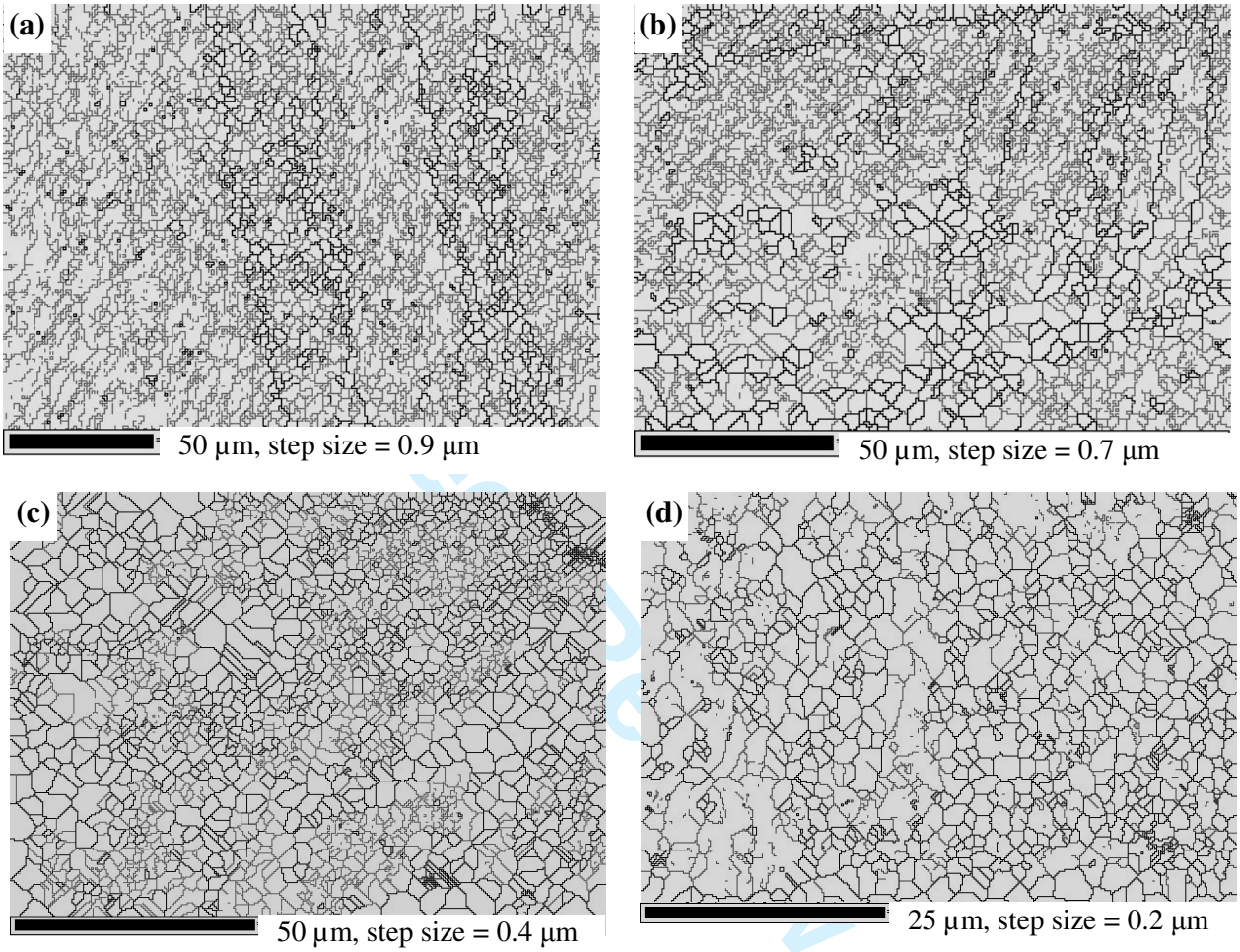

Fig 3

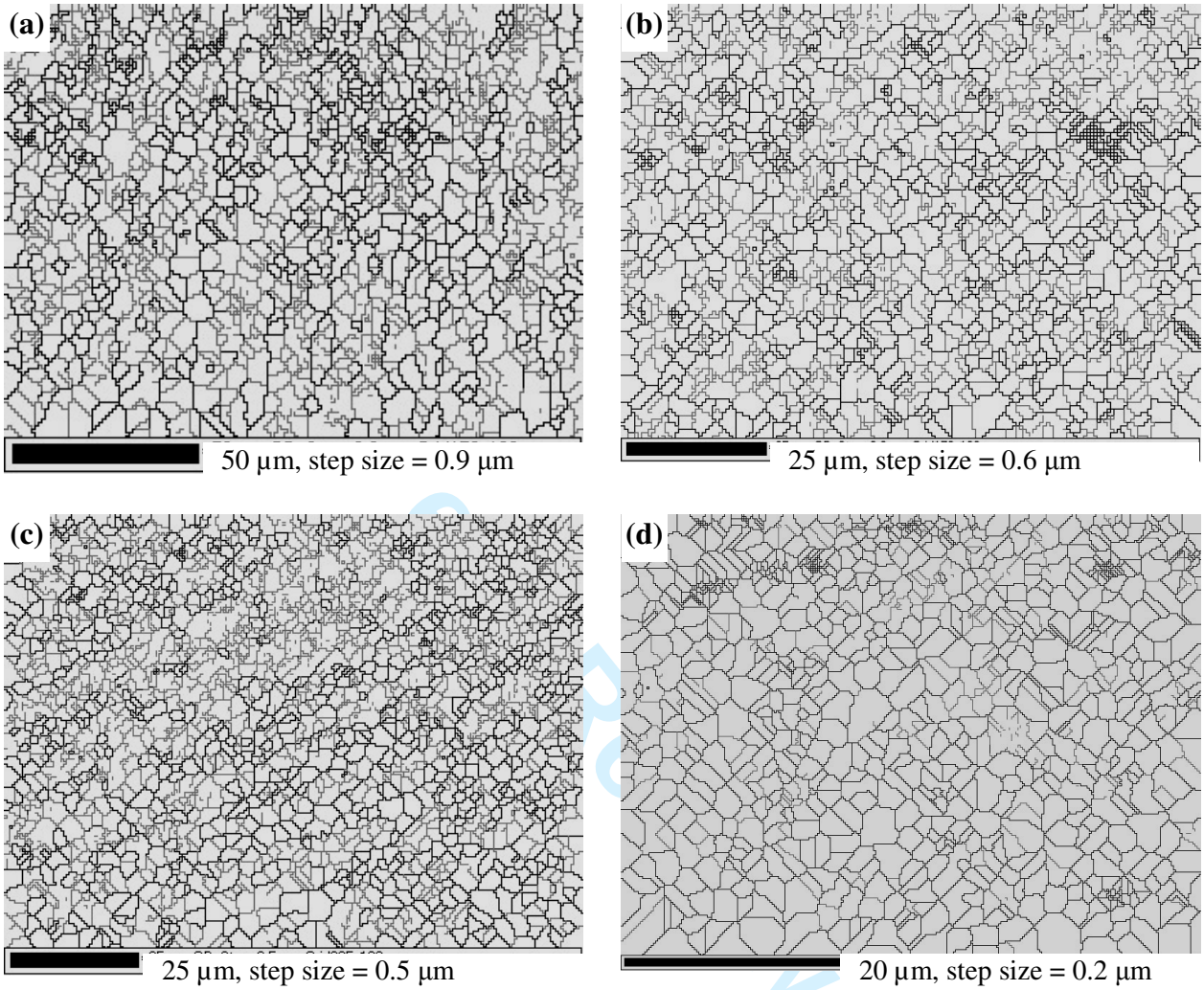

Fig 4

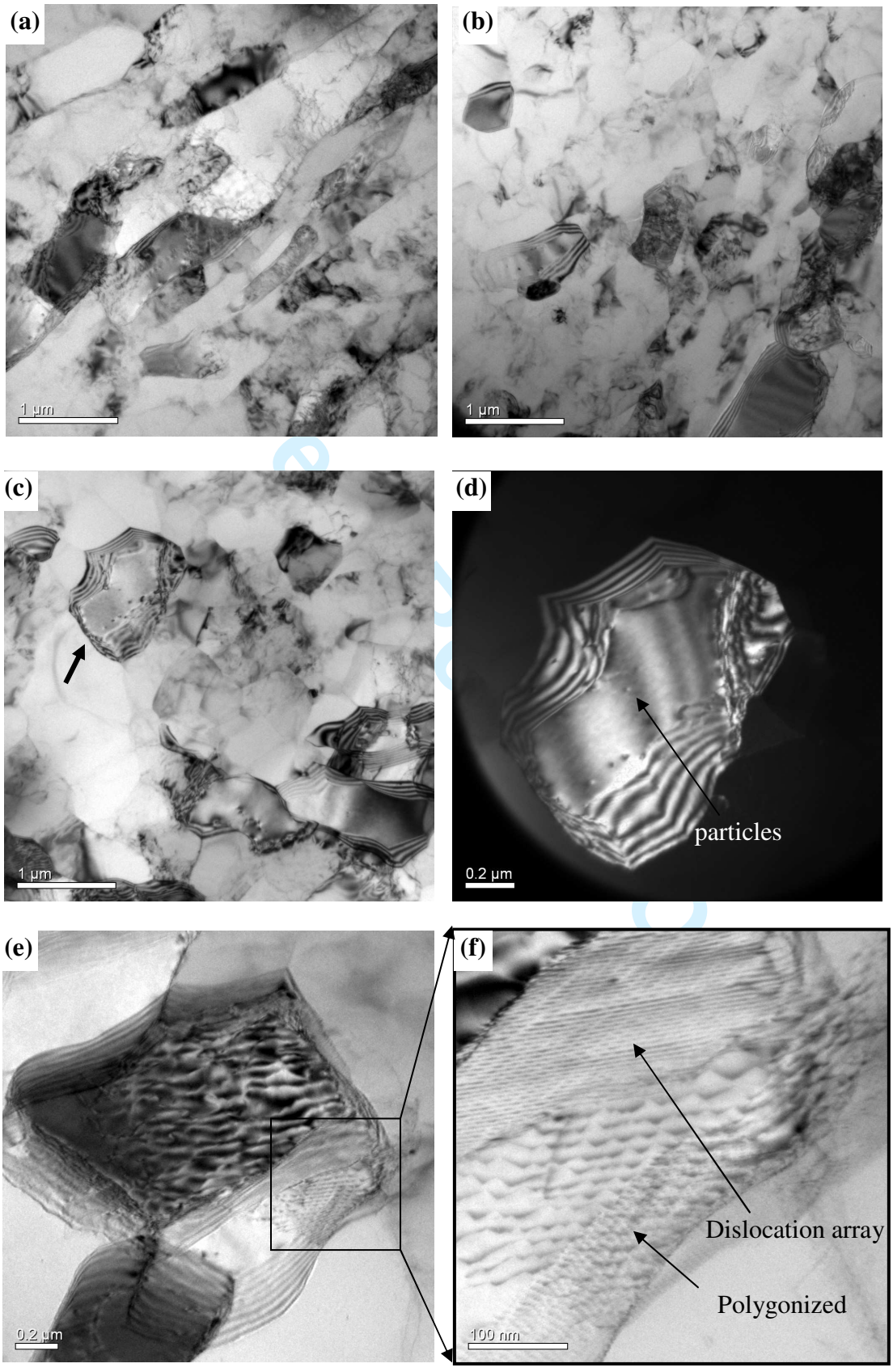
(a)
1 μm
(b)
1 μm
(c)
1 μm
(d)
particles
0.2 μm
(e)
0.2 μm
(f)
Dislocation array
Polygonized
100 nm

Fig 5

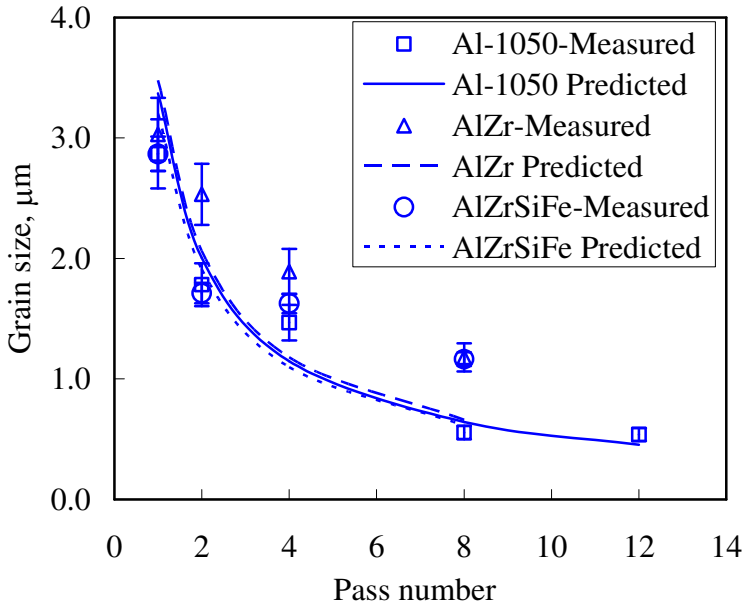

Fig 6

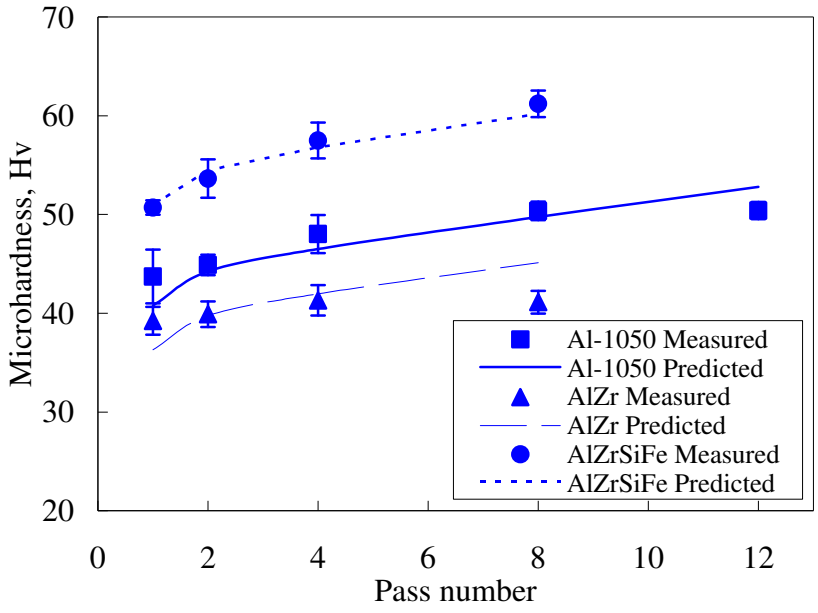

Fig 7

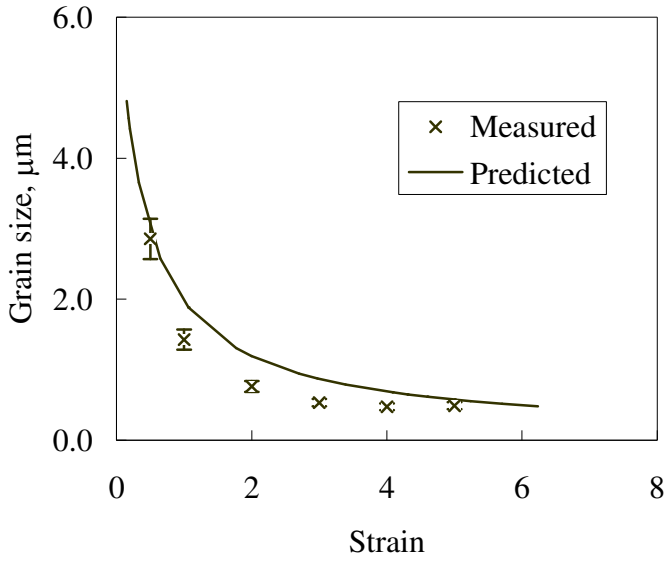

Fig 8

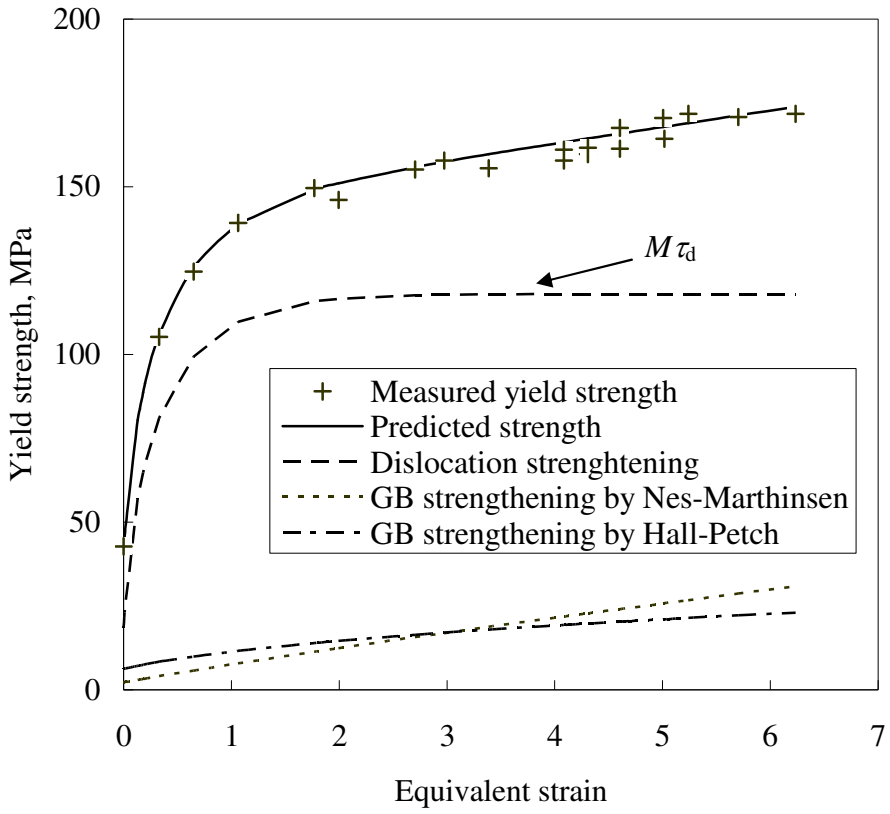

Fig 9

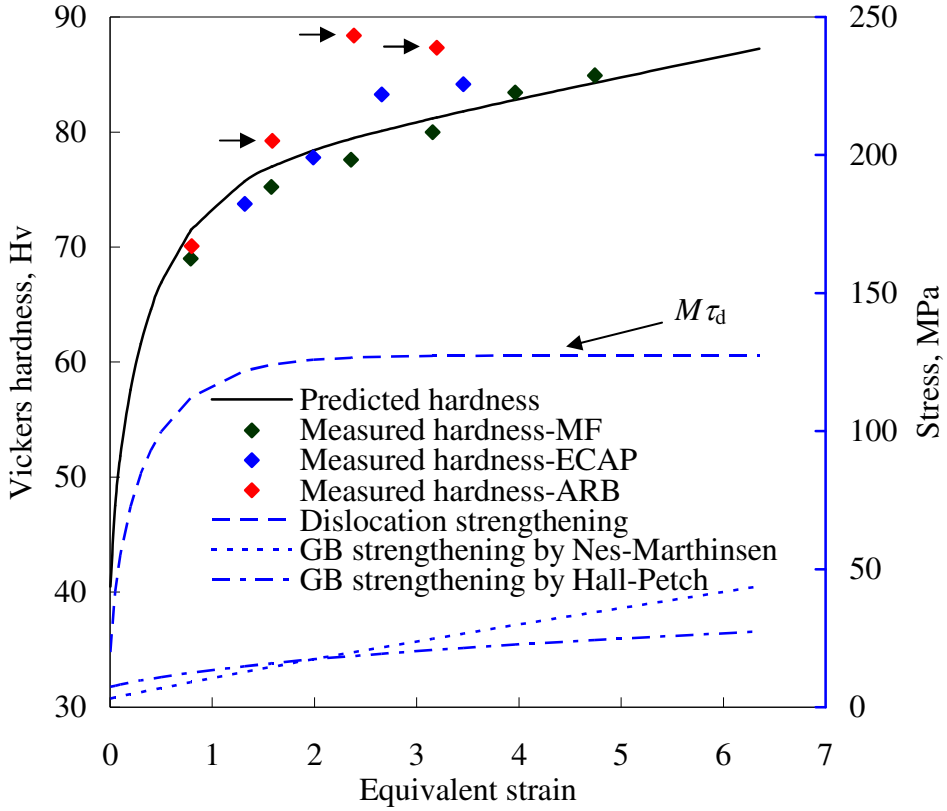

Fig 10

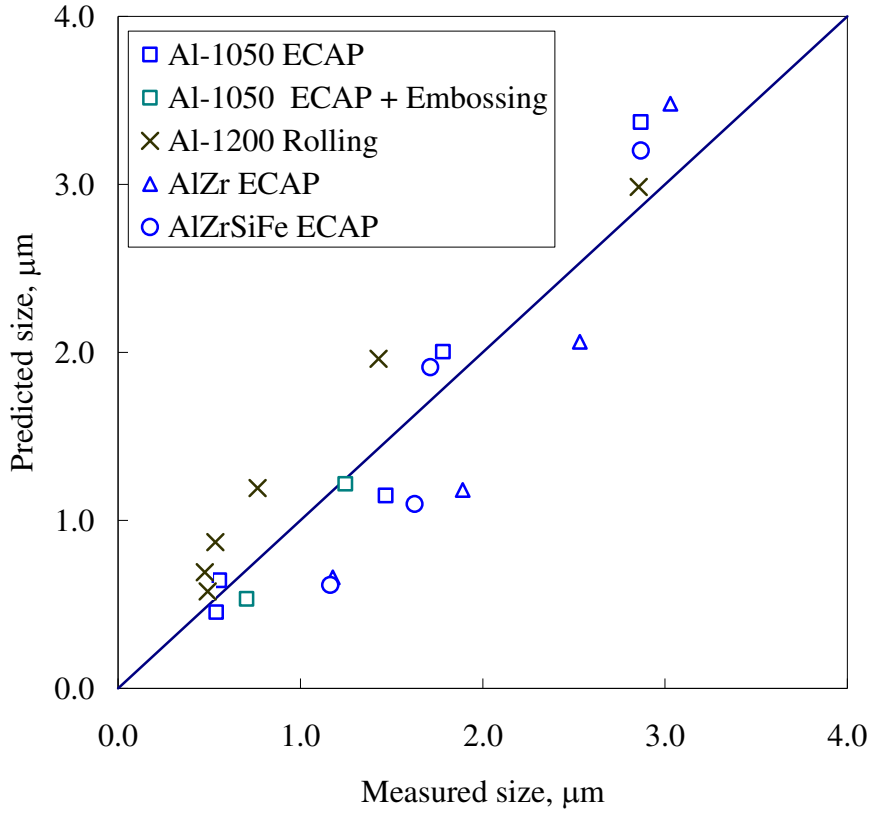

Fig 11

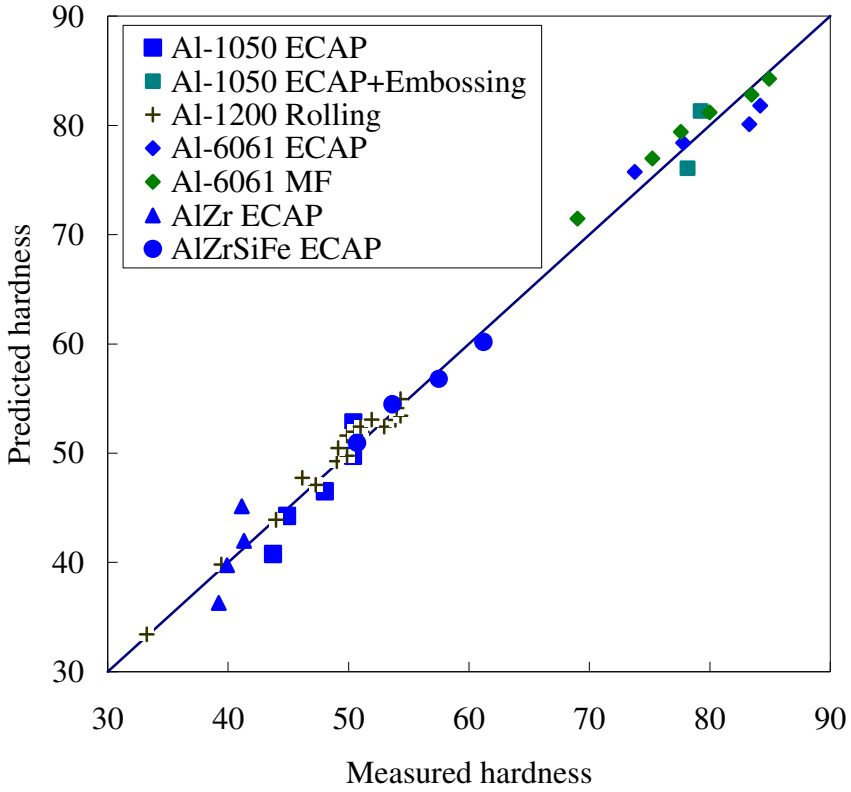

Fig 12